







Light-induced transitions of polar state and domain morphology of photoferroelectric nanoparticlesEugene A. Eliseev ¹, Anna N. Morozovska ^{2,*}, Yulian M. Vysochanskii ³, Lesya P. Yurchenko ¹, Venkatraman Gopalan ^{4,†} and Long-Qing Chen ^{4,‡}¹*Frantsevich Institute for Problems in Materials Science, National Academy of Sciences of Ukraine, Omeliana Pritsaka str., 3, Kyiv, 03142, Ukraine*²*Institute of Physics, National Academy of Sciences of Ukraine, 41, pr. Nauki, 03028 Kyiv, Ukraine*³*Institute of Solid State Physics and Chemistry, Uzhhorod University, 88000 Uzhhorod, Ukraine*⁴*Department of Materials Science and Engineering, Pennsylvania State University, University Park, Pennsylvania 16802, USA*

(Received 24 October 2023; revised 19 December 2023; accepted 9 January 2024; published 26 January 2024)

Using the Landau-Ginzburg-Devonshire approach, we study light-induced phase transitions, evolution of polar state, and domain morphology in photoferroelectric nanoparticles (NPs). Light exposure increases the free-carrier density near the NP surface and may in turn induce phase transitions from the nonpolar paraelectric to the polar ferroelectric phase. Using the uniaxial photoferroelectric $\text{Sn}_2\text{P}_2\text{S}_6$ as an example, we show that visible light exposure induces the appearance and vanishing of striped, labyrinthine, or curled domains and changes in the polarization-switching hysteresis loop shape from paraelectric curves to double, pinched, and single loops, as well as the shifting in the position of the tricritical point. Furthermore, we demonstrate that an ensemble of noninteracting photoferroelectric NPs may exhibit superparaelectric-like features at the tricritical point, such as strongly frequency-dependent giant piezoelectric and dielectric responses, which can potentially be exploited for piezoelectric applications.

DOI: [10.1103/PhysRevB.109.045434](https://doi.org/10.1103/PhysRevB.109.045434)**I. INTRODUCTION**

One of the first experimental pieces of evidence of the photodomain effect was reported in bulk photoferroelectrics in the seminal papers of Fridkin *et al.* [1–3]. Fridkin *et al.* explained the influence of the light exposure on the formation and kinetics of domain structure by the generation of screening charges and photostriction effect. Blouzon *et al.* [4] showed that the photocurrent maps are significantly affected by the presence and configurations of domain walls. It was found that the observed effect is caused by the spatial redistribution of internal electric field associated with the domain walls. Recent dynamic phase-field simulations of the polarization distribution in the $\text{PbTiO}_3/\text{SrTiO}_3$ superlattice before and after ultrafast optical excitation [5–7] revealed the light-induced formation of a ferroelectric supercrystal. Light-driven domain switching is also observed in photochromic ferroelectrics [8].

Note that elastic strains and/or stresses can influence the photoinduced charge-carrier concentration, as well as impede or accelerate their generation. As a rule, this happens because the band gap can change locally under the strain or applied stress. The “weak” change of the band gap can be described in the linear approximation being proportional to the strain (or pressure) coupling with the deformation potential [9,10]. More recent density-functional calculations show that elastic strains can strongly change the band gap of ZnO and TiO_2

oxides [11,12]. It has been predicted theoretically and revealed experimentally that local strains can significantly increase the conductivity of different domain-wall morphologies in ferroelectrics, such as uncharged domain walls [13] and polar vortices [14]. The conducting domain walls and vortex cores appear due to the deformation potential and flexoelectric coupling [14]. Notably, the local energy gap at the ferroelectric domain walls can be different from the bulk gap due to the local strains coupled with the deformation potential and reorientation of the internal atomic coordinates [15], sometimes leading to anomalous photovoltaic effect [16]. It has been revealed that elastic and surface strains can significantly change the optical properties of semiconducting core-shell nanoparticles, Zn-ZnO and ZnO-TiO_2 , due to the local strain-induced changes of the band gap [17]. Recently, the surface charge-mediated transitions of the loop shape from the square to pinched and then to double loops, as well as associated phase boundaries, have been predicted in ferroelectric PbTiO_3 nanoparticles [18].

However, to the best of our knowledge, the photodomain effect in photoferroelectric nanoparticles is little studied theoretically. The interaction of light quanta with an electron-phonon subsystem under nanoscale confinement conditions is of great importance to the development of domain-wall electronics [19] and strain engineering [20–22]. In this work, we employ the $\text{Sn}_2\text{P}_2\text{S}_6$ NPs as a model system to study the photodomain effect.

The $\text{Sn}_2\text{P}_2\text{S}_6$ crystal is a classic example of a photoferroelectric semiconductor with a 2.5-eV band gap, monoclinic symmetry group, Curie temperature $T_C = 338\text{K}$, and spontaneous polarization about $14\ \mu\text{C}/\text{cm}^2$ at room temperature [23]. In the darkness the electric conductivity of $\text{Sn}_2\text{P}_2\text{S}_6$

*Corresponding author: anna.n.morozovska@gmail.com†Corresponding author: vgopalan@psu.edu‡Corresponding author: lqc3@psu.edu

crystals is of the hole type, the position of the acceptor level with respect to the valence band is about 0.1 eV, and the electron-type conductivity appears under the visible light illumination. The photoconductive and photovoltaic properties of $\text{Sn}_2\text{P}_2\text{S}_6$ were determined by Vysochanskii *et al.* [23,24] and Cho *et al.* [25], respectively. Spectroscopy and temperature dependences of photocurrents in $\text{Sn}_2\text{P}_2\text{S}_6$ were studied by Sotome *et al.* [26], and an evident correlation between the photovoltaic effect and the spontaneous polarization was established. It was recently shown that the polarization dynamics in $\text{Sn}_2\text{P}_2\text{S}_6$ and related ferroelectric materials are governed by the effective multiwell free-energy landscape of the long-range polar order [27].

We define the physical problem and present the Landau-Ginzburg-Devonshire (LGD) approach in Sec. IIA. We then analyze the light-induced phase transitions, accompanied by transformations of polar state, domain morphology, and hysteresis loops in photoferroelectric NPs in Secs. IIB and IIC. We discuss possible applications of the NPs in Sec. IIIA and present our conclusions in Sec. IIIB. The Supplemental Material [28] contains the detailed mathematical formulation of the problem, description of the methods, a table of material parameters employed in the calculations, and auxiliary figures of results.

II. THEORETICAL MODELING

A. Basic equations

The LGD free energy (G_{LGD}) of a ferroelectric NP is the sum of the Landau-Devonshire free energy (g_{LD}), the gradient energy (g_G), the electrostatic energy (g_{El}), the linear elastic energy (g_{EE}), electrostriction (g_{ES}), and flexoelectric (g_{FL}) contributions:

$$G_{\text{LGD}} = \int (g_{\text{LD}} + g_G + g_{\text{El}} + g_{\text{ES}} + g_{\text{FL}}) dx^3, \quad (1a)$$

$$g_{\text{LD}} = \alpha_i P_i^2 + \beta_{ij} P_i^2 P_j^2 + \gamma_{ijk} P_i^2 P_j^2 P_k^2, \quad (1b)$$

$$g_G = g_{ijkl} \frac{\partial P_i}{\partial x_j} \frac{\partial P_k}{\partial x_l}, \quad (1c)$$

$$g_{\text{El}} = -\frac{1}{2} \varepsilon_0 \varepsilon_{ij}^b E_i E_j - E_i P_i, \quad (1d)$$

$$g_{\text{EE}} = -\frac{s_{ijkl}}{2} \sigma_{ij} \sigma_{kl}, \quad (1e)$$

$$g_{\text{ES}} = -Q_{ijkl} P_i P_j \sigma_{kl} - Z_{ijklmn} P_i P_j P_k P_l \sigma_{mn} - \frac{W_{ijklmn}}{2} P_i P_j \sigma_{mn} \sigma_{kl}, \quad (1f)$$

$$g_{\text{FL}} = +\frac{F_{ijkl}}{2} \left(\sigma_{ij} \frac{\partial P_k}{\partial x_l} - P_k \frac{\partial \sigma_{ij}}{\partial x_l} \right). \quad (1g)$$

The integration in Eq. (1a) is performed over the volume of NP. The values α_i , β_{ij} , and γ_{ijk} in Eq. (1b) are the Landau-Devonshire expansion coefficients. The coefficient α_i depends linearly on the temperature T , $\alpha_i(T) = \alpha_T(T - T_C)$, where T_C is the Curie temperature of a bulk ferroelectric. Other coefficients in Eq. (1b) are temperature independent. The values g_{ijkl} in Eq. (1c) are the components of the polarization gradient tensor. In Eq. (1d) E_i is the electric field, ε_0 is a

vacuum dielectric permittivity, and ε_{ij}^b are the components of background dielectric constant tensor [29]. Hereinafter we regard the background as isotropic, $\varepsilon_{ij}^b = \varepsilon_b \delta_{ij}$, where δ_{ij} is a Kronecker delta symbol. Values σ_{ij} in Eq. (1e) are the components of a stress tensor, $i, j = 1-3$. The values Q_{ijkl} , Z_{ijklmn} , and W_{ijklmn} denote the components of a linear and two nonlinear electrostriction strain tensors, respectively [30,31]. The values F_{ijkl} in Eq. (1f) are the components of a flexoelectric tensor. An Einstein summation convention over repeated indices is employed herein.

The quasistatic electric field E_i is related to the electric potential ϕ through $E_i = -\frac{\partial \phi}{\partial x_i}$. The electric potential ϕ satisfies the Poisson equation inside the photoferroelectric NP:

$$-\varepsilon_0 \varepsilon_b \delta_{ij} \frac{\partial^2}{\partial x_i \partial x_j} \phi = e(n_h - n_e - N_a^- + N_d^+) - \frac{\partial P_i}{\partial x_i}, \quad (2a)$$

where e is the absolute value of electron charge; n_e and n_h , N_a^- and N_d^+ are, respectively, the concentration of free electrons and holes, and photoionized acceptors and donors, which obey the charge transport equations (see Appendix A in Ref. [28], and Refs. [32–36] therein for details). We assume that Boltzmann statistics is valid for nondegenerate charge carriers in thermodynamic equilibrium, and that the global electroneutrality condition is satisfied under a continuous light exposure. We also neglect heating effects related with the light exposure assuming that they are either small for small intensities of light or/and compensated by effective cooling of the NPs. Unfortunately, we did not find the tensors of deformation potential, flexoelectric coupling, and surface tension coefficients for $\text{Sn}_2\text{P}_2\text{S}_6$, and therefore did not consider the pressure influence on the band structure of $\text{Sn}_2\text{P}_2\text{S}_6$ core-shell NPs, leaving this important question for future studies.

Due to the surface band bending induced by the “bare” (i.e., unscreened) depolarization field, we assume that the thickness of surface layer enriched by photoionized carriers is very small, and the carriers can effectively decrease the bare depolarization field in the layer in a self-consistent manner. Therefore, we can use the approximation $|e\phi| \ll k_B T$ and thus the Debye-Hückel approximation for the bulk charge density, $\rho_b = e(n_h - n_e - N_a^- + N_d^+)$, inside the layer:

$$\rho_b \approx \frac{2e^2 n_e}{k_B T} \phi. \quad (2b)$$

Here, k_B is the Boltzmann constant. Using the approximation (2b), Eq. (2a) transforms into the Debye-type equation inside the layer. Outside the layer, as well as outside the NP, $\rho_b \approx 0$, so ϕ satisfies the Laplace-type equation there. Equations (2a) and (2b) are supplemented by the continuity condition of the electric potential ϕ and electric displacements \vec{D} at the particle surface (see Appendix B in Ref. [28], and Refs. [37–43] therein for details). Since the thickness of surface layer enriched by photoionized carriers can be very small, one can solve the Laplace-type equation, $-\delta_{ij} \frac{\partial^2}{\partial x_i \partial x_j} \phi = \frac{1}{\varepsilon_0 \varepsilon_b} \frac{\partial P_i}{\partial x_i}$, instead of using Eq. (2a), and use the following boundary conditions for ϕ and \vec{D} :

$$(\phi_{\text{ext}} - \phi_{\text{int}})|_S = 0, \quad \vec{e}_S (\vec{D}_{\text{ext}} - \vec{D}_{\text{int}})|_S = -\frac{\varepsilon_0 \phi}{L_D}. \quad (2c)$$

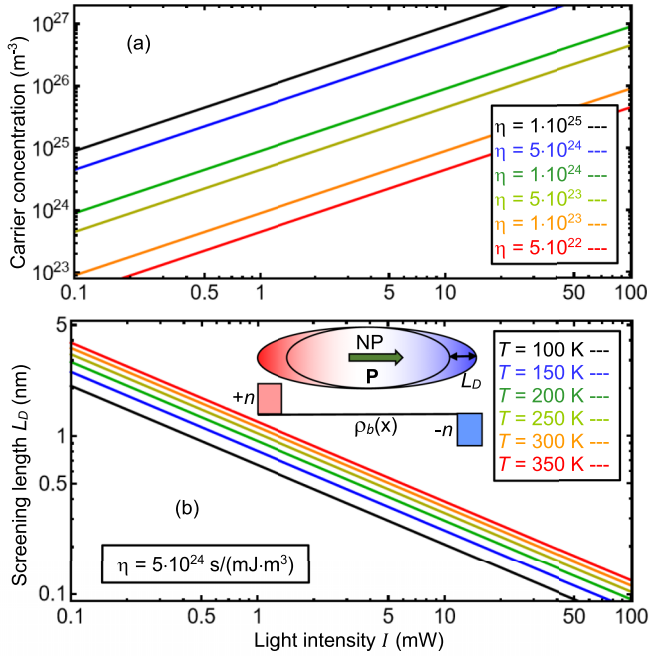


FIG. 1. The dependence of the concentration n of photoionized charge carriers (a) and the screening length L_D (b) on the intensity I of visible light. Plot (a) is calculated for several η values, which vary from 10^{25} to 5×10^{22} s/(mJ m³), and $T = 300$ K (see legend). Plot (b) is calculated for several temperatures: $T = 100, 150, 200, 250, 300,$ and 350 K (see legend), and the factor η is equal to 5×10^{24} s/(mJ m³). Background permittivity $\epsilon_b = 9$ and $c_0 \leq 10^{22}$ m³ correspond to the photoferroelectric Sn₂P₂S₆.

In Eq. (2c) \vec{e}_S is the normal to the NP surface S , and L_D is the Debye-Hückel screening length. The length is given by the expression $L_D = \sqrt{\frac{k_B T \epsilon_0 \epsilon_b}{2e^2 n}}$, where n is the free-carrier concentration under illumination at $\varphi = 0$. Hereinafter, the letter “ n ” can denote the concentration of electrons (n_e) in electron-type photoferroelectrics, or holes (n_h) in hole-type photoferroelectrics, or the total concentration of free carriers in intrinsic photoferroelectrics. Due to the light-induced increase in the free-carrier density, the concentration n and the length L_D strongly depend on the light intensity I , namely:

$$n \approx n_0 + \tau_n(\chi + \gamma_p N_p)I, L_D \approx \sqrt{\frac{k_B T \epsilon_0 \epsilon_b}{2e^2 [c_0 + \tau_c(\chi + \gamma_p N_p)I]}}. \quad (3)$$

Here, n_0 is the free-carrier (electrons and/or holes) concentration in the darkness and τ_n is the lifetime of photoionized carriers. N_p is the concentration of photoactive atoms (acceptors or/and donors), γ_p is their photoionization coefficient, and χ is the reduced photovoltaic glass constant. The derivation of Eq. (3) is given in Appendixes A and B in Ref. [28].

The dependence of the concentration n on the intensity I is shown in Fig. 1(a) for several values of the parameter $\eta = \tau_n(\chi + \gamma_p N_p)$. As one can see, n increases from 10^{23} to 10^{28} m⁻³ with increase in I from 0.1 to 100 mW. The dependence of the screening length L_D on the temperature T and light intensity I is shown in Fig. 1(b). For a realistic set of

parameters, corresponding to the photoferroelectric Sn₂P₂S₆ (band gap 2.5 eV, light wavelength 440–500 nm), L_D changes from 5 nm to 1 Å with increase in I .

Polarization dynamics in an external field follows from minimization of the LGD free energy (1), and corresponding time-dependent LGD equations have the form

$$\Gamma \frac{\partial P_i}{\partial t} = - \frac{\delta G_{\text{LGD}}}{\delta P_i}. \quad (4a)$$

Here, Γ is the Khalatnikov kinetic coefficient [44]. The boundary condition for P_i at the nanoparticle surface S is “natural,” i.e.,

$$g_{ijkl} e_{sk} \frac{\partial P_i}{\partial x_l} \Big|_S = 0. \quad (4b)$$

The time-dependent LGD equations (4a) and (4b) should be solved self-consistently with the Poisson equation (2a), where the concentration of free electrons and holes, photoionized acceptors, and donors obey the time-dependent charge-transport equations (A2) listed in Appendix A in Ref. [28].

B. Light-induced changes of polar states and domain morphology

In order to study the light-induced changes of phase diagrams, domain morphology, and related effects in photoferroelectric Sn₂P₂S₆ NPs, we perform finite-element modeling (FEM) in COMSOL@MULTIPHYSICS software. The COMSOL@MULTIPHYSICS model uses the electrostatics module for the solution of the Poisson equation (2a), solid mechanics, and general math (PDE TOOLBOX) modules for the self-consistent solution of time-dependent LGD equations (4a) and (4b) and the charge-transport equations (A2) of the drift-diffusion type. Material parameters of Sn₂P₂S₆ are listed in Table CI in Appendix C in Ref. [28], and Refs. [45–53] therein for details.

FEM is performed for ellipsoidal Sn₂P₂S₆ NPs with different sizes and aspect ratios, discretization densities of the self-adaptive tetragonal mesh, and initial polarization distributions (e.g., randomly small fluctuations or polydomain states). The NPs are placed inside the rectangular parallelepiped-shaped cell filled with an optically transparent dielectric with the dielectric permittivity ϵ_e . The main sizes of the parallelepiped are bigger for each dimension than the axes of the ellipsoidal core-shell NP. We tried to use the hyperfine computational mesh inside the NP and fine enough outside it. To reach the goal, we used the cubic computational cell for a spherical nanoparticle, prolate or oblate parallelepipeds for prolate and oblate ellipsoids, respectively (see Fig. B1 in Appendix B in Supplemental Material [28]).

Final stable structures were obtained after a long simulation time, $t \gg 10^3 \tau$, where the parameter τ is the Landau-Khalatnikov relaxation time, $\tau = \Gamma/|\alpha(0)|$. The considered system reaches the minimum (local or global) of the LGD free energy (1) in the thermodynamic equilibrium. Since most kinetic parameters in the drift-diffusion equations (A2) are poorly known (or even unknown in many cases), we use an adiabatic approximation being interested in the thermodynamic equilibrium state only. The latter consists of the solution of the time-dependent LGD equations (4a) and (4b), together with the Debye-Hückel approximation (2b) in

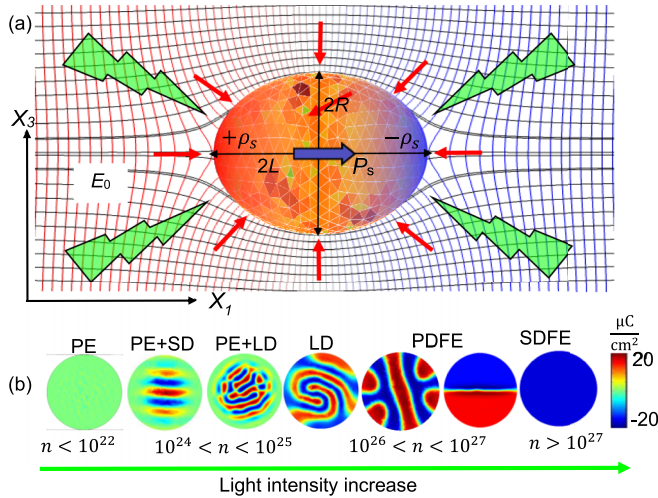


FIG. 2. (a) An ellipsoidal NP with semiaxes R and L . The smallest mesh elements, used in FEM, have a light-green color, larger elements are orange and red, and the largest have a dark-red color. The spontaneous polarization P_s , shown by a blue arrow, is directed along the ellipsoidal axis L and induces the screening charge near the NP surface, which density is ρ_s . The NP is placed in a homogeneous quasistatic electric field \vec{E}_0 codirected with its polar axis X_1 . Red arrows illustrate the direction of the hydrostatic pressure σ application (e.g., compression, $\sigma > 0$, is shown). Light-green zigzag arrows illustrate the continuous laser exposure. (b) Typical relaxed distributions of spontaneous polarization in the equatorial $\{X_2, X_3\}$ cross section of the stress-free ellipsoidal $\text{Sn}_2\text{P}_2\text{S}_6$ NP with radius $R \cong 15$ nm and aspect ratio $0.5 \leq \frac{R}{L} \leq 1.5$ calculated for different ranges of n (in m^{-3}) and $T \ll T_C$. Abbreviations: PE denotes the paraelectric phase, LD is for labyrinthine domains, PDFE is for the polydomain ferroelectric state, and SDFE is for the single-domain ferroelectric state.

the Poisson equation (2a), being consistent with the global electroneutrality condition under a continuous light exposure.

The ellipsoidal NP with semiaxes R and L is schematically shown in Fig. 2. The spontaneous polarization, P_s , shown by a blue arrow, is directed along its polar axis “ X_1 ,” which coincides with the ellipsoid semi-axis L . The spontaneous polarization induces the screening charge near the NP surface, the density ρ_s of which is equal to $-\frac{\epsilon_0 \phi}{L_D}$ in accordance with Eq. (2c). The NP is placed in a homogeneous quasistatic electric field \vec{E}_0 codirected with the axis X_1 . Red arrows illustrate the direction of the hydrostatic pressure application. Light-green zigzag arrows illustrate the light exposure.

Ellipsoidal $\text{Sn}_2\text{P}_2\text{S}_6$ NPs can exhibit several phases or states, which are the paraelectric (PE) phase, the single-domain ferroelectric (SDFE) state, and the polydomain ferroelectric (PDFE) state. The domain morphology, which can be striped domains (SD), labyrinthine domains (LD), curved domains of complex shape, or bidomains, is dependent on the concentration n of screening carriers in the surface layer, which is in turn determined by the light intensity. Typical light-induced changes of polarization distribution in the equatorial cross section of the stress-free ellipsoidal NP as n increases (i.e., with the light-intensity increase) are shown in Fig. 2(b). The PE phase at first transforms to the mixed PE+SD state, then to the mixed PE+LD state, next to the LD

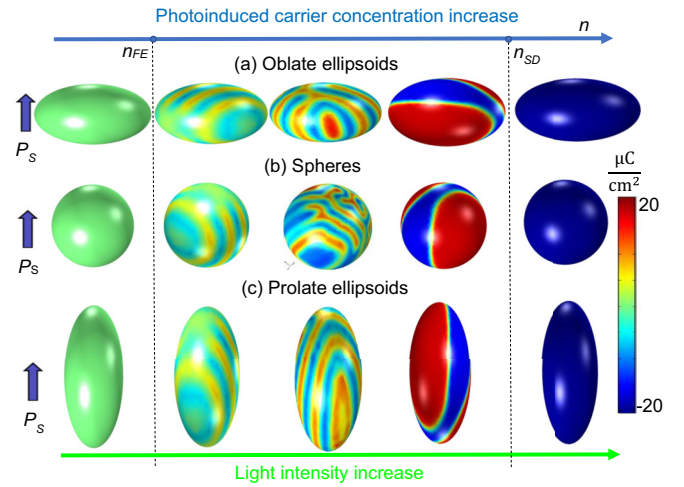


FIG. 3. A relaxed domain morphology of the stress-free ellipsoidal $\text{Sn}_2\text{P}_2\text{S}_6$ NP calculated at $T \ll T_C$ and different values of n , which increases from 10^{22}m^{-3} (left column) to 10^{28}m^{-3} (right column). The images (a) show oblate ellipsoids with an aspect ratio $R/L = 3/2$ (a); the images (b) show nanospheres with $R/L = 1$; and the images (c) show prolate ellipsoids with an aspect ratio $R/L = 2/3$. The spontaneous polarization direction is shown by a blue arrow. The color scale shows the polarization value in $\mu\text{C}/\text{cm}^2$. Material parameters of $\text{Sn}_2\text{P}_2\text{S}_6$ are listed in Table CI in Appendix C in Supplemental Material [28].

and PDFE states, and eventually to the SDFE state as n increases from 10^{22} to 10^{28}m^{-3} . The increase in n corresponds to the light-intensity increase from ~ 0.1 to 10 mW according to Eq. (3) and Fig. 1.

Typical relaxed domain morphologies of the stress-free ellipsoidal NPs calculated at temperatures below Curie temperature, $T < T_C$, and very long relaxation time, $t \gg 10^3 \tau$, are shown in Fig. 3. The polarization state of nanoellipsoids, schematically shown in Fig. 3, at first undergoes a continuous transition from the PE phase to the fine-striped PDFE or LD states; then, the domain period becomes bigger, and eventually the transition to the SDFE state occurs with increase in n from 10^{22}m^{-3} (dark conductivity) to 10^{28}m^{-3} (metallic conductivity). Concentrations n_{FE} and n_{SD} correspond to the onset of domain formation and to the transition from the PDFE state to the SDFE state, respectively.

Since the concentration n of photoionized carriers in the surface layer is linearly proportional to the light intensity I in accordance with Eq. (3), the light exposure can induce the phase transitions from the nonpolar PE to the polar FE states, and the changes of domain morphology in the FE state, which opens the possibilities of light control of the domain states in ferroelectric NPs.

The changes in domain morphology caused by light exposure (i.e., the “photodomain effect”) critically depends on the temperature, NP sizes (R and L), shape (aspect ratio R/L), and applied pressure. Even for stress-free ellipsoidal NPs, some of which are shown in Fig. 4, the light-induced evolution of domain morphology is very complex, and, in order to establish some general trends, a huge amount of FEM simulations is required (see, e.g., Figs. D1–D3 in Appendix D in Ref. [28]). FEM, performed for oblate, spherical, and prolate NPs with

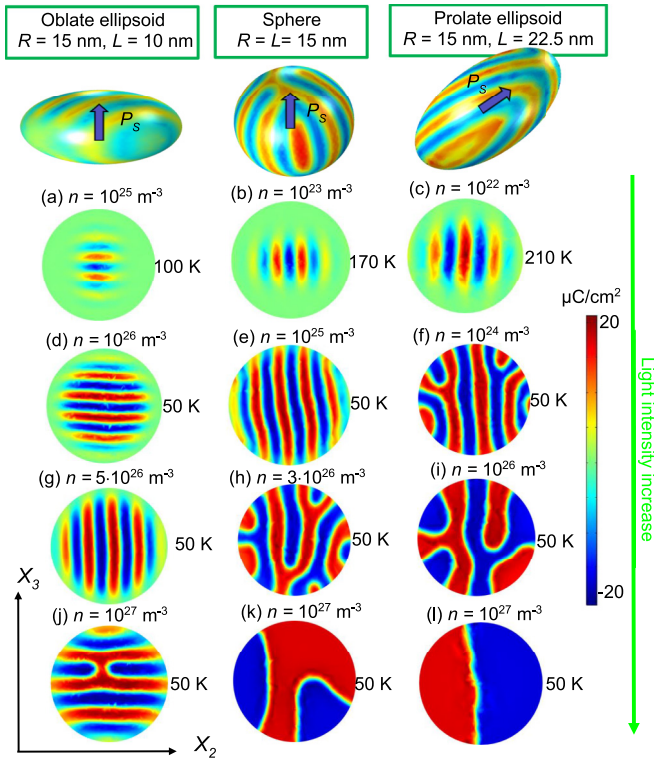


FIG. 4. Relaxed spontaneous polarization P_1 in the equatorial cross section $\{X_2, X_3\}$ of the stress-free ellipsoidal NPs calculated for different concentrations n (listed in the plots in m^{-3}), temperatures T (listed in the plots in K), and sizes $R = 15$ nm, $L = 10$ nm (left column), $R = L = 15$ nm (middle column), and $R = 15$ nm, $L = 22.5$ nm (right column). The simulation time $t \gg 10^3 \tau$. The spontaneous polarization direction is shown by a blue arrow. Material parameters of $\text{Sn}_2\text{P}_2\text{S}_6$ are listed in Table CI in Appendix C in Ref. [28].

the same radius, $R \cong (10 - 20)$ nm, in the temperature range (50–300) K, reveals the following trends:

(a) The examples demonstrating the onset of domain formation are shown in Figs. 4(a), 4(b), and 4(c) at definite temperature-dependent concentration n_{FE} for temperatures T_{FE} below the Curie temperature T_C and NP sizes above the critical sizes. The value of n_{FE} decreases in several orders of magnitude (e.g., from 10^{25} to 10^{22}m^{-3}), and corresponding transition temperature T_{FE} increases in a hundred of kelvin (e.g., from 100 to 200 K) when the NP shape changes from oblate to prolate (e.g., from $R/L = 3/2$ to $R/L = 2/3$). This trend originated from a significant decrease in the depolarization field contribution with decrease in R/L . Indeed, much smaller n_{FE} is required to screen the polarization bound charge accumulated near the remote poles of a strongly prolate NP in comparison with much higher n_{FE} required for the compensation of bound charges located at the large-area faces of an oblate NP. Quantitative explanations will be given in the next section using analytical expressions for the depolarization factor n_d , since the inequality $n_d^{\text{needle}} \ll n_d^{\text{sphere}} \ll n_d^{\text{disk}}$ is valid for the polarization orientation shown in Figs. 3 and 4.

(b) The domain morphology at the domain onset (i.e., at $n \cong n_{\text{FE}}$) looks similar for all studied shapes and presents itself the small-amplitude domain stripes, located in the central

part of the NP and surrounded by the thick “shell” of the PE phase, that can be classified as the coexisting PE and PDFE regions. The domain onset with shape-independent morphology is explained by the dominant contribution of the polarization gradient energy (which determines the energy of uncharged domain walls) to the total free energy in comparison with smaller Landau-Devonshire energy and depolarization field energy. The free-energy minimum, reached under the optimal balance of these three contributions, determines the value of n_{FE} for a given shape and sizes.

(c) For concentrations n which are 1–2 orders of magnitude higher than n_{FE} and low temperatures, $T \ll T_C$, the domain morphology varies from multiple slightly curved domain stripes to meandering stripes, then to labyrinthine domains and/or irregular curved polydomains in dependence on the NP shape [see examples in Figs. 4(d)–4(h)]. For concentrations n , which are 3–4 orders of magnitude higher than n_{FE} and close to n_{SD} , we observed several curved domains, bidomain and single-domain states [see examples in Figs. 4(i)–4(l)]. Most studied NPs are single domains for $n \geq 10^{28} \text{m}^{-3}$ and $T \leq (200 - 300)$ K. Oblate and spherical NPs are paraelectric for $n \leq (10^{23} - 10^{25}) \text{m}^{-3}$ and $T \geq (100 - 200)$ K.

(d) The concentration range, $n_{\text{FE}} < n < n_{\text{SD}}$, is the smallest for oblate NPs (see the left column in Fig. 4), bigger for spherical NPs (see the middle column in Fig. 4), and the biggest for prolate NPs (see the right column in Fig. 4). The appearance of fine domain stripes is most likely for oblate NPs with the aspect ratio $R/L \geq 1.5$, while other types of domain structure are unlikely for the NP shape. Fine stripes, labyrinthine domains, and curved domains are characteristic for spherical and quasispherical NP with the aspect ratio $0.8 < R/L \leq 1.2$. The region of wide domain stripes and bidomains significantly increases for prolate NPs with the aspect ratio $R/L < 1.5$.

Note that the information obtained by FEM and presented in Fig. 4 and Figs. D1–D3 is far from being sufficient to create a complete physical picture of the light-induced changes of phase state and domain formation in ellipsoidal photoferroelectric NPs. Analytical expressions for the critical concentrations, transition temperatures, and phase boundaries are required.

C. Analytical expressions for the phase boundaries in ellipsoidal nanoparticles

Analytical expressions for the phase boundaries can be derived only for uniaxial ferroelectric NPs with either spherical, or prolate, or oblate ellipsoidal shapes [54,55]. Below, we analyze approximate analytical expressions for the boundaries between the PE phase, PDFE and SDFE states for ellipsoidal ferroelectric NPs, the relatively high accuracy of which have been corroborated by FEM.

Approximate expression for the temperature of the PE phase instability with respect to the single-domain polarization appearance is [55]

$$T_{\text{PE-SDFE}} = T_C + \frac{2\sigma_{ij}}{\alpha_T} \left(Q_{11ij} + \frac{1}{2} W_{11ijkl} \sigma_{kl} \right) - \frac{n_d \varepsilon_0^{-1}}{\alpha_T [\varepsilon_b n_d + \varepsilon_e (1 - n_d) + n_d (L/L_D)]}. \quad (5a)$$

The first term in Eq. (5a) is a bulk Curie temperature; the second term originates from electrostriction coupling with elastic stress. We only consider the case of hydrostatic pressure, $\sigma_{11} = \sigma_{22} = \sigma_{33} = -\sigma$, since the case is the easiest to realize experimentally for an ensemble of NPs. Note that the surface tension can renormalize the nonzero stress components, σ_{ii} , as $\sigma_{33} = -\sigma - \frac{\mu}{R}$, $\sigma_{22} = -\sigma - \frac{\mu}{R}$ and $\sigma_{11} = -\sigma - \frac{\mu}{L}$ [56], where $\mu \cong (1-3)$ N/m is a relatively small surface-tension coefficient [57,58]. In order to focus on the influence of external pressure, we further neglect the surface tension by setting $\mu = 0$ in this work. The temperature (5a) corresponds to the PE-SDFE transition if $(\beta - 4Z_{1111ij}\sigma_{ij}) > 0$. For the case $(\beta - 4Z_{1111ij}\sigma_{ij}) < 0$, the PE-SDFE transition occurs at the temperature $T_{SDFE} = T_{PE-SDFE} + \frac{1}{4\gamma\alpha_T}(\beta - 4Z_{1111ij}\sigma_{ij})^2$.

The third term in Eq. (5a) is the contribution of a depolarization field, which also depends on the dielectric permittivity of NP surrounding, ε_e . The term, depending on the ratio L/L_D , strongly suppresses the PE-SDFE transition temperature for small disks and vanishes for long needles being proportional

$$T_{PE-PDFE} = T_C + \frac{\sigma_{ij}}{\alpha_T}(2Q_{11ij} + W_{11ijkl}\sigma_{kl}) - \frac{1}{\alpha_T} \left(gk_m^2 + \frac{n_d\varepsilon_0^{-1}}{[\varepsilon_b n_d + \varepsilon_e(1-n_d)](1+L^2k_m^2) + n_d(L/L_D)} \right). \quad (6a)$$

The first two terms in Eq. (6a) are the same as in Eq. (5a); the third and fourth terms in parentheses originate from the correlation effect and depolarization field energy of the domain stripes, respectively. Here, $g = g_{1212}$ or $g = g_{2323}$ independent of the direction of wave vector k_m of the domain structure onset in the polar cross section. Under the condition $(\beta - 4Z_{1111ij}\sigma_{ij}) < 0$, the PE-PDFE transition occurs at the temperature $T_{PDFE} = T_{PE-PDFE} + \frac{1}{4\gamma\alpha_T}(\beta - 4Z_{1111ij}\sigma_{ij})^2$.

The minimal, i.e., the ‘‘threshold,’’ value of k_m , is size dependent and screening dependent, but temperature independent:

$$k_m = \frac{1}{L} \sqrt{\frac{L}{L_{cr}} - 1}. \quad (6b)$$

The corresponding domain period is $D_m = \frac{2\pi}{k_m}$. From Eq. (6), the PE-PDFE transition occurs only if the NP size L in polar direction is bigger than the critical size, $L > L_{cr}$. For $L < L_{cr}$ the PE-SDFE transition happens. The critical size is shape dependent and screening dependent:

$$L_{cr} = \left(\sqrt{\frac{n_d\varepsilon_0^{-1}}{g[\varepsilon_b n_d + \varepsilon_e(1-n_d)]}} - \frac{n_d}{[\varepsilon_b n_d + \varepsilon_e(1-n_d)]L_D} \right)^{-1}. \quad (6c)$$

to L_D/L . Since L_D is T - and n dependent, and n is proportional to light intensity I in accordance with Eq. (3), expression (5a) is the equation for determination of the $T_{PE-SDFE}$ dependence on σ , n , and I .

The dimensionless parameter n_d is the shape-dependent depolarization factor [59]:

$$n_d(\xi) = \frac{1-\xi^2}{\xi^3} \left(\ln \sqrt{\frac{1+\xi}{1-\xi}} - \xi \right). \quad (5b)$$

Here, $\xi = \sqrt{1 - (\frac{R}{L})^2}$ is the eccentricity ratio of the ellipsoid.

An approximate analytical expression for the NP transition temperature from the PDFE to the PE phase can be derived using the approach described in Appendix B of Ref. [54]. Under the condition $(\beta - 4Z_{1111ij}\sigma_{ij}) > 0$, the corresponding equation for the $T_{PE-PDFE}$ dependence on stresses σ_{ij} , sizes R and L , concentration n , and light intensity I , has the form

Expressions (6a) and (6b) are physical under the condition

$$\sqrt{\frac{n_d\varepsilon_0^{-1}}{g[\varepsilon_b n_d + \varepsilon_e(1-n_d)]}} \geq \frac{1}{L} + \frac{n_d}{[\varepsilon_b n_d + \varepsilon_e(1-n_d)]L_D}. \quad (7)$$

At fixed gradient coefficient g the equality in Eq. (7) means that the relation between the particle semilength L and effective screening length L_D should be valid for the domain onset.

The equality in Eq. (7) corresponds to the transition to the single-domain state that occurs in a triple point on the phase diagram, where the energies of the SDFE and PDFE states are equal to zero energy of the PE phase. In the triple point, $T_{PE-PDFE} = T_{PE-SDFE}$ allowing for Eqs. (5a) and (6a). Hence, the equations for the determination of triple-point temperature (T_{tr}) and concentration (n_{tr}) for a given length L are

$$T_{tr} = T_C + \frac{2\sigma_{ij}}{\alpha_T} \left(Q_{11ij} + \frac{1}{2} W_{11ijkl}\sigma_{kl} \right) - \frac{n_d\varepsilon_0^{-1}}{\alpha_T[\varepsilon_b n_d + \varepsilon_e(1-n_d) + n_d(L/L_D)]}, \quad (8a)$$

$$\frac{1}{L} = \sqrt{\frac{n_d\varepsilon_0^{-1}}{g[\varepsilon_b n_d + \varepsilon_e(1-n_d)]}} - \frac{n_d}{[\varepsilon_b n_d + \varepsilon_e(1-n_d)]L_D}, \quad (8b)$$

where $L_D = \sqrt{\frac{k_B T_{tr} \varepsilon_0 \varepsilon_b}{2e^2 n_{tr}}}$. Exclusion of L_D from Eqs. (8a) and (8b) leads to the expressions for the T_{tr} and n_{tr} :

$$T_{tr} = T_C + \frac{2\sigma_{ij}}{\alpha_T} \left(Q_{11ij} + \frac{1}{2} W_{11ijkl}\sigma_{kl} \right) - \frac{\sqrt{n_d g}}{\alpha_T L \sqrt{\varepsilon_0[\varepsilon_b n_d + \varepsilon_e(1-n_d)]}}, \quad (9a)$$

$$n_{tr} = \frac{k_B T_{tr} \varepsilon_0 \varepsilon_b}{2e^2} \left(\sqrt{\frac{[\varepsilon_b n_d + \varepsilon_e(1-n_d)]}{\varepsilon_0 g n_d}} - \frac{[\varepsilon_b n_d + \varepsilon_e(1-n_d)]}{n_d L} \right)^2. \quad (9b)$$

Expression for the NP transition temperature from the PDFE to the SDFE state follows from the equality of these phases' free energies since the transition is of the first order. Approximate analytical expressions are absent in this case, and the PDFE-SDFE boundary can be established from FEM. For most cases the PDFE-SDFE boundary is very close to the continuation of the PE-SDFE curve below the triple point, and sometimes almost coincides with it.

Below, we analyze the dependence of NP phase diagrams on the temperature T , pressure σ , and concentration n of photoionized carriers near the surface of the NP. Phase diagrams as a function of n and T calculated for $\sigma = 0$ are shown in Figs. 5(a), 5(c), and 5(e). Phase diagrams as a function of n and σ calculated for $T = 298$ K are shown in Figs. 5(b), 5(d), and 5(f). All these diagrams contain the region of PE phase, the region of SDFE state, and the wide region of PDFE state lying between the PE and the SDFE regions. The PE phase, PDFE, and SDFE states coexist in the triple point, which is shown by a black circle in most of the diagrams. The diagrams are sensitive to the ellipsoid aspect ratio R/L . In particular, the diagrams calculated for nanodisks and nanospheres are

quantitatively different, and they are qualitatively different from the diagrams of nanoneedles, as discussed below.

The diagrams in Fig. 5(a) and 5(b) are calculated for the $\text{Sn}_2\text{P}_2\text{S}_6$ nanodisks with radius $R = 150$ nm and semiheight $L = 15$ nm. Stress-free nanodisks, diagram of which is shown in Fig. 5(a), are PE at the temperatures above (125 – 270) K, and their transition temperature from the PE phase to the PDFE state increases from 125 to 250 K with increase in n from 10^{24} to 10^{28} m^{-3} . The transition temperature from the PDFE to the SDFE state increases from 5 to 240 K with increase in n from 10^{24} to 10^{28} m^{-3} . The coordinates of the triple point are $\{225 \text{ K}, 10^{28} \text{ m}^{-3}\}$. Stressed nanodisks, diagram of which is shown in Fig. 5(b), are PE for the tensions $\sigma > -(0.72 - 0.1)$ GPa and room temperature. The critical pressure of the PE-PDFE transition increases from -0.72 to -0.3 GPa with increase in n from 10^{24} to 10^{28} m^{-3} . The critical pressure of the PDFE-SDFE transition increases from -1 to -0.3 GPa with increase in n from 2×10^{27} to 10^{28} m^{-3} . The triple point has coordinates $\{-0.3 \text{ GPa}, 10^{28} \text{ m}^{-3}\}$.

The diagrams in Figs. 5(c) and 5(d) are calculated for the $\text{Sn}_2\text{P}_2\text{S}_6$ nanospheres with radius $R = 15$ nm. The phase diagram of stress-free nanosphere is shown in Fig. 5(c), which indicate the thermodynamic state is PE at the temperatures above (210 – 280) K, and the transition temperature from the PE phase to the PDFE state increases from 210 to 280 K with increase in n from 10^{24} to 10^{28} m^{-3} . The transition temperature from the PDFE to the SDFE state increases from 5 to 280 K with increase in n from 10^{24} to 10^{28} m^{-3} . The triple-point coordinates are $\{275 \text{ K}, 10^{28} \text{ m}^{-3}\}$. The phase diagram of stressed nanospheres is shown in Fig. 5(d), which indicates that the thermodynamic states are PE for the tensions $\sigma > -(0.42 - 0.1)$ GPa and room temperature. The critical pressure of the PE-PDFE transition increases from -0.72 to -0.3 GPa with increase in n from 10^{24} to 10^{28} m^{-3} . The critical pressure of the PDFE-SDFE transition increases from -1 to -0.3 GPa with increase in n from 2×10^{27} to 10^{28} m^{-3} . The triple point has coordinates $\{-0.3 \text{ GPa}, 3 \times 10^{28} \text{ m}^{-3}\}$.

The diagrams in Figs. 5(e) and 5(f) are calculated for the $\text{Sn}_2\text{P}_2\text{S}_6$ nanoneedles with radius $R = 15$ nm and semilength $L = 150$ nm. For stress-free nanoneedles, the phase diagram in Fig. 5(e) shows that the thermodynamic states are PE at the temperatures above 332 K. The transition temperature from the PE phase to the PDFE state is independent on n due to the very small depolarization factor of the nanoneedles with $R/L \ll 1$. The PDFE state is stable below 332 K, and the transition temperature from the PDFE to the SDFE state increases from 200 to 330 K with increase in n from 10^{24} to 10^{28} m^{-3} . The triple point should be located at $\{332 \text{ K}, 10^{29} \text{ m}^{-3}\}$, but it is not shown in Fig. 5(e), because $n = 10^{29} \text{ m}^{-3}$ corresponds to the metal state. Stressed nanoneedles, diagram of which is shown in Fig. 5(f), are PE for the tensions $\sigma > -0.15$ GPa and room temperature. The critical pressure of the PE-PDFE transition is n independent: the PDFE state is stable below -0.15 GPa. The critical pressure of the PDFE-SDFE transition increases from -0.35 to -0.15 GPa with increase in n from 10^{24} to 10^{28} m^{-3} . The triple point should be located at $\{-0.15 \text{ GPa}, 10^{29} \text{ m}^{-3}\}$, but it is not shown in Fig. 5(f) due to the unrealistically high n .

The increase in photoionized carrier concentration n for a given temperature can lead to the transition from the PE phase

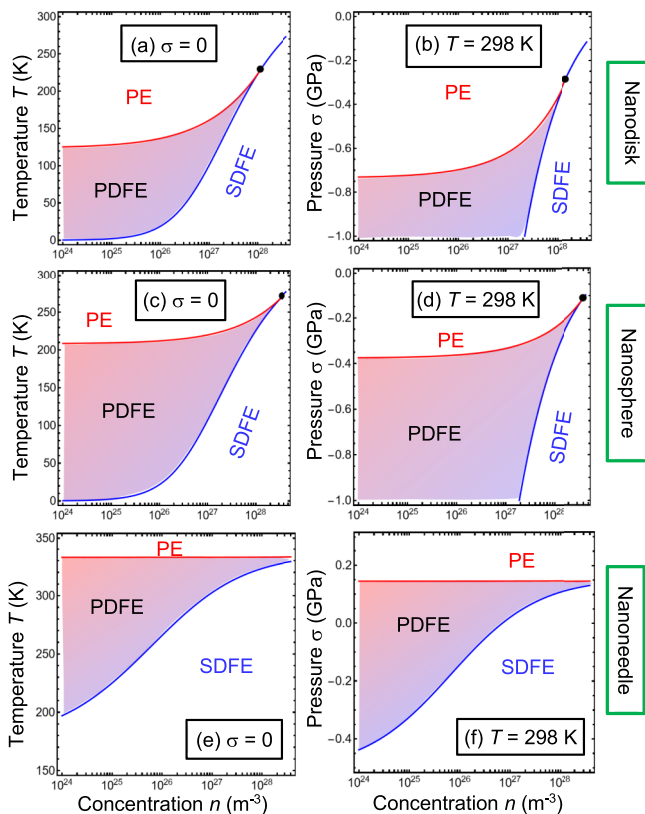


FIG. 5. (a), (c), (e) Phase diagrams as a function of photoionized carrier concentration n and temperature T . (b), (d), (f) Phase diagrams as a function of concentration n and pressure σ . The diagrams (a), (b) are calculated for the $\text{Sn}_2\text{P}_2\text{S}_6$ nanodisk with radius $R = 150$ nm and semiheight $L = 15$ nm; (c), (d) are for the nanosphere with radius $R = 15$ nm; and (e), (f) are for the nanoneedle with radius $R = 15$ nm and semilength $L = 150$ nm. The triple point is shown by a black circle. Material parameters of $\text{Sn}_2\text{P}_2\text{S}_6$ are listed in Table CI in Appendix C in Ref. [28].

to the PDFE state, and then to the SDFE state in nanodisks and nanospheres [see Figs. 5(a) and 5(b)]. Also, the increase in n for a given temperature can lead to the transition from the PDFE state to the SDFE state in nanoneedles [see Figs. 5(e) and 5(f)]. Since n is proportional to the light intensity in accordance with Eq. (3), the light-induced phase transitions from the nonpolar PE phase to the polar FE states, as well as the phase diagram control by light exposure, are possible in the ellipsoidal ferroelectric NPs.

D. Polarization dependence on applied electric field

To analyze the polarization field dependence, $P_1(E_0)$, we regard that the NP is placed in a homogeneous quasistatic electric field \vec{E}_0 along its polar axis. Polarization dynamics in external field follows from Eq. (4):

$$\Gamma \frac{\partial P_1}{\partial t} + [\alpha - \sigma_{ij}(2Q_{11ij} + W_{11ijkl}\sigma_{kl})]P_1 + (\beta - 4Z_{1111ij}\sigma_{ij})P_1^3 + \gamma P_1^5 - g_{11ij} \frac{\partial^2 P_1}{\partial x_i \partial x_j} = E_1. \quad (10a)$$

In Eq. (10a), the electric field \vec{E} is a superposition of external field \vec{E}_0 and depolarization field \vec{E}_d , created by the uncompensated bound charges (ferroelectric dipoles) near the particle surface [60] and charged domain walls (if any exist). The natural boundary condition for P_1 at the NP surface S acquires the form

$$g_{11ij} e_{Si} \left. \frac{\partial P_1}{\partial x_j} \right|_S = 0, \quad (10b)$$

where \vec{e}_S is the outer normal to the ellipsoid surface. In order to analyze a quasistatic polarization reversal, we regard that the frequency ω of sinusoidal external field E_0 is very small in comparison with the Landau-Khalatnikov relaxation time, $\tau = \Gamma/|\alpha(0)|$, e.g., the product $\omega\tau \ll 10^{-3}$.

As shown earlier [61], the domain structure appearance and its morphology in the FE state depend strongly on the magnitude and anisotropy of the polarization gradient coefficients, g_{ijkl} . For $\text{Sn}_2\text{P}_2\text{S}_6$, several times increase in g_{ijkl} above $10^{-10}\text{Jm}^3/\text{C}^2$ can suppresses the domain formation in the FE state. In this case and allowing for the natural boundary conditions (10b), polarization gradient effects can be neglected in the single-domain state.

The FEM performed for parameters listed in Table CI in Appendix C in Supplemental Material [28] shows that the $\text{Sn}_2\text{P}_2\text{S}_6$ NPs undergo both polydomain and single-domain polarization-switching scenarios above the critical sizes. The case of polydomain polarization switching does not allow any sort of analytical description, and should be simulated by FEM. The case of single-domain polarization switching allows an analytical description, and the shape of the single-domain loop is defined by the structure of the LGD potential (1). In order to study the role of the photoionized carriers and pressure on the polarization switching in the NPs, we analyze Eqs. (10a) and (10b) for the single-domain polarization-switching scenario.

The field dependence of a quasistatic single-domain polarization can be found from the following equation:

$$\Gamma \frac{\partial P_1}{\partial t} + \alpha^* P_1 + \beta^* P_1^3 + \gamma P_1^5 = E. \quad (11)$$

Here, $\beta^* = \beta - 4Z_{1111ij}\sigma_{ij}$, and E is an external field inside the NP, which can differ from applied field, E_0 , due to the dielectric and screening effects. The depolarization field, E_d , and stresses, σ_i , contribute to the “renormalization” of coefficient $\alpha(T)$, which becomes the temperature-, stress-, shape-, size-, and light intensity-dependent function α^* :

$$\alpha^* = \alpha(T) + \frac{n_d \varepsilon_0^{-1}}{\alpha_T [\varepsilon_b n_d + \varepsilon_e (1 - n_d) + n_d (L/L_D)]} - 2\sigma_{ij} \left(Q_{11ij} + \frac{1}{2} W_{11ijkl} \sigma_{kl} \right). \quad (12)$$

The derivation of the second term in Eq. (12) is given in Ref. [62]. Here, $L_D(T, n)$ is given by Eq. (3). Assuming that the band bending is small for the small magnitude of E_0 , the density of free charges, induced by E_0 , is relatively small too, and so the estimate $E \approx \frac{\varepsilon_s E_0}{\varepsilon_b n_d + \varepsilon_s (1 - n_d)} \cong E_0$ [63] is valid for $\varepsilon_e \cong \varepsilon_b$.

The diagrams in Figs. 6(a)–6(g) illustrate a typical influence of the photoionized carrier concentration n , temperature T , and hydrostatic pressure σ on the shape of quasistatic hysteresis loops, $P_1(E)$, calculated for ellipsoidal $\text{Sn}_2\text{P}_2\text{S}_6$ NPs. The diagrams as a function of n and T calculated for $\sigma = 0$ are shown in Figs. 6(a), 6(c), and 6(e). The diagrams as a function of n and σ calculated for $T = 298$ K are shown in Figs. 6(b), 6(d), and 6(f). The diagrams contain a red region of paraelectric curves (PC), an orange region of double loops (DL), a light-green region of pinched loops (PL), and blue and cyan regions of single loops (SL), which have a simple or a complex structure of static curves, respectively. The shapes of hysteresis loops (solid curves) and corresponding static curves (black dashed curves) are shown in Fig. 6(g). Their detailed classification, which takes into account the loop shape and the structure of the static curves, is given in Ref. [63]. The diagrams’ view is sensitive to the ellipsoid aspect ratio R/L . The diagrams calculated for nanodisks [shown in Figs. 6(a) and 6(b)] and nanospheres [shown in Figs. 6(c) and 6(d)] look quantitatively different, and they both are qualitatively different from the diagrams calculated for nanoneedles [shown in Figs. 6(e) and 6(f)].

The loop diagrams in Fig. 6 are “isomorphous” to the phase diagrams in Fig. 4, as anticipated. In particular, red PC regions in Fig. 6 exactly coincide with the PE phase regions in Fig. 4; wide blue and thin cyan SL regions in Fig. 6 together completely fill the SDFE state regions in Fig. 4; and orange DL regions and light-green PL regions in Fig. 6 together completely fill the PDFE state regions in Fig. 4. The area of DL regions is significantly bigger than the area of PL regions; and the boundary between these regions is diffuse. Very thin cyan regions of SLs exist for nanodisks and nanospheres; they are absent for nanoneedles. The isomorphism of quasistatic hysteresis loops shape (Fig. 6) and phase diagrams (Fig. 4) is natural, because any polarization bistability (and thus any loops) are absent in the PE phase, whereas only single loops can exist in the SDFE state. The DLs and PLs, as well as loops of more complex shape, can exist in the PDFE state only.

The increase in the photoionized carrier concentration n for a given temperature can lead to the transition from the PC curves to the DLs, PLs, and then to the SLs in nanodisks and nanospheres, as well as to the DL-PL-SL transitions in

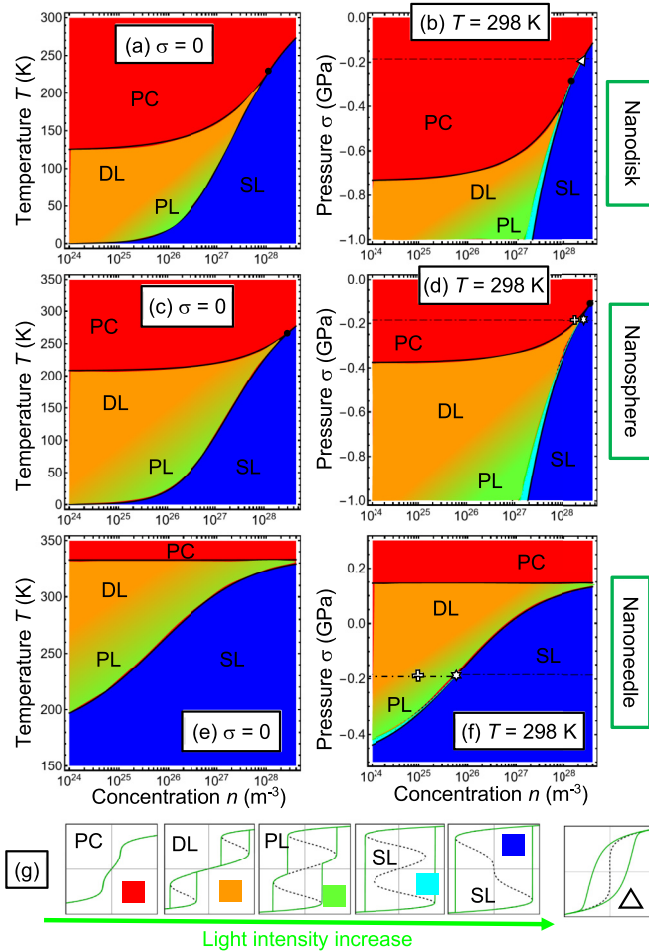


FIG. 6. (a), (c), (e) The shape of quasistatic hysteresis loops, $P_1(E)$, as a function of photoionized carrier concentration n and temperature T . (b), (d), (f) The shape of quasistatic hysteresis loops, $P_1(E)$, as a function of concentration n and pressure σ . The plots (a), (b) are calculated for the $\text{Sn}_2\text{P}_2\text{S}_6$ nanodisk with radius $R = 150$ nm and semiheight $L = 15$ nm; (c), (d) are for the nanosphere with radius $R = 15$ nm; and (e), (f) are for the nanoneedle with radius $R = 15$ nm and semilength $L = 150$ nm. The dotted-dashed horizontal line is $\beta^* = 0$. The triple point is shown by a black circle, and the tricritical point in the plot (b) is shown by a white triangle; white crosses and stars in the plots (d) and (f) indicate the points of morphological transitions in the domain structure. Color scale: red is paraelectric curves (PC), orange is double loops (DL), light green is pinched loops (PL), cyan and blue are single loops (SL). (g) The shape of hysteresis loops (solid curves) and corresponding static curves (black dashed curves). Material parameters of $\text{Sn}_2\text{P}_2\text{S}_6$ are listed in Table CI in Appendix C in Ref. [28].

nanoneedles (see Fig. 6). Since n is proportional to the light intensity in accordance with Eq. (3), the light-induced changes of polarization-switching scenario and hysteresis loop shape are possible in the ferroelectric NPs.

The tricritical point [64], where β^* and α^* simultaneously change their signs, is shown by a white triangle in Fig. 6(b). The point is the cross of the dotted-dashed horizontal line, $\beta^* = 0$, and the black solid curve, $\alpha^* = 0$. The rightmost loop in Fig. 6(g) corresponds to the tricritical point, where the slope

of polarization static curves is almost vertical, and the width of quasistatic hysteresis loop of polarization is very sensitive to the frequency of applied field. The effect originates from the critical lowering of the polarization-switching energy barrier when approaching the tricritical point. Since the position of the tricritical point is n dependent, as shown in Fig. 6(b), the light exposure can shift the point to the working (e.g., room) temperature, and thus significantly decrease the NP coercivity and increase electric and piezoelectric permeability in the point. The light-driven shift of the tricritical point can be important for advanced applications of the photoferroelectric NPs, and the possibility is discussed in the next section.

The points of morphological phase transitions in the domain structure [54,61] are shown by white crosses and stars in Fig. 6(d) (for spheres) and Fig. 6(f) (for needles). The points are the cross of the dashed horizontal line, $\beta^* = 0$ (corresponding to “critical” pressure $\sigma = -0.185$ GPa), and the boundaries separating different polarization-switching scenarios, namely the PC curves, DLs, PLs, and SLs. The quasistatic hysteresis loops $P_1(E)$, calculated for spherical $\text{Sn}_2\text{P}_2\text{S}_6$ NPs in the points of morphological phase transitions, shown in Fig. 6(d), look similar to the rightmost loop in Fig. 6(g) calculated in the tricritical point. This is because the cross and the star are very close to one another in Fig. 6(d); due to the very small α^* in the region of diagram, the polarization behavior in the points of morphological phase transitions is very close to the behavior in the tricritical point, where $\alpha^* = 0$ and $\beta^* = 0$. In contrast, the loops $P_1(E)$, calculated for prolate $\text{Sn}_2\text{P}_2\text{S}_6$ NPs in the points of morphological phase transitions, shown in Fig. 6(f), are very different from the loop in Fig. 6(g). This is because the cross and the star are far from one another in Fig. 6(f); also, the region of diagram is very far from the condition $\alpha^* = 0$.

Notably, the surface charge-mediated transitions of the loop shape from the square to pinched and then to double loops, as well as associated phase boundaries, were predicted earlier by Mangeri and co-workers [18] in ferroelectric PbTiO_3 nanoparticles (see, e.g., Figs. 1 and 3 in Ref. [18]). Their calculations assumed that the relative permittivity differs from vacuum outside the nanoparticle [18].

III. DISCUSSION

A. Possible applications of the light-driven shift of the tricritical point

Quasistatic hysteresis loops of polarization, $P_1(E)$, relative dielectric permittivity, $\varepsilon_{11}(E)$, piezoelectric coefficients, $d_{11}(E)$ and $d_h(E)$, calculated at the tricritical point of the $\text{Sn}_2\text{P}_2\text{S}_6$ nanodisk, are shown in Fig. 7 (see also Fig. E1 in Appendix E in Supplemental Material [28]). The tricritical point is shifted to the room temperature by the hydrostatic pressure and light exposure. Dotted black curves are the static dependences; red, brown, green, and blue loops correspond to very low frequencies of applied field, $\omega\tau = 10^{-7}$, 10^{-6} , 10^{-5} , and 10^{-4} , respectively. The slope of polarization static curves is almost vertical, and the coercivity of quasistatic hysteresis loops of polarization, dielectric permittivity, and piezoelectric coefficients are very sensitive to the frequency of applied field. The permittivity and piezoelectric

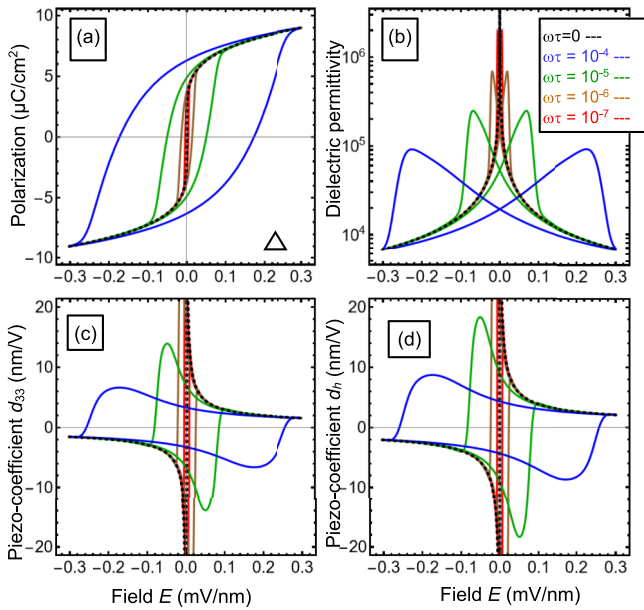


FIG. 7. (a) Quasistatic hysteresis loops of polarization $P_3(E)$; (b) dielectric permittivity $\varepsilon_{33}(E)$, piezoelectric coefficients $d_{33}(E)$ (c) and $d_h(E)$; and (d) calculated for the $\text{Sn}_2\text{P}_2\text{S}_6$ nanodisk with radius $R = 150$ nm, semiheight $L = 15$ nm, and several very low frequencies of applied field $\omega\tau = 10^{-7}$, 10^{-6} , 10^{-5} , 10^{-4} (red, brown, green, and blue loops). Dotted black curves are the static dependences. Temperature $T = 298$ K, concentration $n = 2 \times 10^{28} \text{ m}^{-3}$, and $\sigma = -0.185$ GPa correspond to the tricritical point. Material parameters of $\text{Sn}_2\text{P}_2\text{S}_6$ are listed in Table CI in Appendix C in Ref. [28].

coefficients can reach giant values not only near the coercive field, where the static dependences diverge, but also far from it. In particular, ε_{11} can be more than 10^5 and d_{11} can be more than 5 nm/V for zero and very small values of applied electric field. The ultrahigh sensitivity of quasistatic hysteresis loops coercivity to the frequency value and significant enhancement of ε_{11} and d_{11} originate from the vanishing of the polarization-switching energy barrier in the tricritical point, resulting in the “critical slowing down effect.”

We would like to emphasize that the quasistatic hysteresis loops of $P_1(E)$, $\varepsilon_{11}(E)$, $d_{11}(E)$, and $d_h(E)$, calculated for oblate $\text{Sn}_2\text{P}_2\text{S}_6$ NPs with the aspect ratio $10 < R/L < 1$, $R = 15$ nm, $T = 298$ K, concentrations $n = (1-2)10^{28} \text{ m}^{-3}$, and “critical” pressure $\sigma = -0.185$ GPa corresponding to $\beta^* = 0$, look very similar to the loops shown in Fig. 7. This is because these loops correspond either to the tricritical point, similar to those shown in Fig. 6(b), or to the points of morphological phase transitions, similar to those shown in Fig. 6(d), which are close to one another due to the small $\alpha^* \rightarrow 0$. Indeed, the condition $\alpha^* \rightarrow 0$ provides the proximity to the point of the paraferroelectric transition. Despite the high concentration range, $n = (1-2)10^{28} \text{ m}^{-3}$, required for the effect observation, it is quite possible, because the photoionized carriers are located in an ultrathin surface layer of thickness $\sim L_D$.

Since the position of the tricritical point and the points of morphological phase transitions are n dependent, the

light exposure can be used to tune them to significantly increase the dielectric permittivity and piezoelectric coefficients at the required (e.g., room) temperature. Exposed to light, polar behavior of an ensemble of noninteracting (or weakly interacting) stressed photoferroelectric NPs can reveal superparaelectric-like features at the working temperature, such as strongly frequency-dependent giant piezoelectric and dielectric responses. Hence, the self-assembled arrays of oblate photoferroelectric NPs (such as nanoflakes or nanopills) can be used as basic elements in photosensitive piezoelectric actuators, as well as in piezoelectric transformers of solar energy for, e.g., energy harvesting.

B. Conclusions

Using the Landau-Ginzburg-Devonshire approach, we study light-induced phase transitions and the accompanying transformations of polar state and domain morphology in photoferroelectric NPs. Due to the light-induced increase in the free-carrier density near the NP surface, the effective Debye-Hückel screening length strongly depends on the light intensity. Since the concentration of photoionized carriers is proportional to the intensity, the light exposure induces phase transitions from the nonpolar paraelectric phase to the polar ferroelectric state and thus the changes of domain morphology and phase diagrams of free and stressed NPs.

In particular, the continuous exposure by visible light can control the formation and disappearance of domain stripes, labyrinths and meanders, curved polydomains, bidomains, and single-domain states in the ellipsoidal NPs of uniaxial photoferroelectric $\text{Sn}_2\text{P}_2\text{S}_6$. Also, the light exposure can induce strong changes in polarization-switching hysteresis loop shapes in the $\text{Sn}_2\text{P}_2\text{S}_6$ NPs from paraelectric curves to double-, pinched-, and single loops.

The light exposure can shift the position of the morphological transition(s) and/or tricritical point to the working (e.g., room) temperature, where the energy barrier of polarization switching can be very low (for pills) or vanish (for disks and nanoflakes). When exposed to light, polar, dielectric and piezoelectric responses of an ensemble of noninteracting (or weakly interacting) stressed photoferroelectric NPs can reveal superparaelectric-like features at this special point, such as strongly frequency-dependent giant piezoelectric and dielectric responses, which may be utilized for advanced piezoelectric applications.

Analytical and numerical results presented in the work were obtained and visualized using a specialized software, *Mathematica 13.1* [65], and the *Mathematica* notebook, which contain the codes, and are available per reasonable request.

ACKNOWLEDGMENTS

The work is supported by the U.S. Department of Energy, Office of Science, Basic Energy Sciences, under Award No. DE-SC0020145 as part of the Computational Materials Sciences Program. E.A.E. and L.P.Y. are also supported by the National Academy of Sciences of Ukraine (Basic Research Program No. 0122U000808 “New physical phenomena in multiferroics on the base of oxides and chalcogenides for modern nanoelectronics and spintronics”). A.N.M. also

acknowledges funding from the National Academy of Sciences of Ukraine (Grant No. 4.8/23-п, Innovative materials and systems with magnetic and/or electro-dipole ordering for the needs of using spintronics and nanoelectronics in strategically important issues of new technology). This research was in part (A.N.M. and L.P.Y.) sponsored by the NATO Science for Peace and Security Programme under Grant No. SPS G5980 "FRAPCOM." The authors are very grateful to

the Referee for the simulating discussions and very useful suggestions.

Research idea belongs to A.N.M, Yu.M.V. and L.-Q.C.; A.N.M. formulated the problem, performed analytical calculations, analyzed results, and wrote the manuscript draft; E.A.E. wrote codes and prepared figures jointly with L.P.Y.; and Yu.M.V., V.G., and L.-Q.C. worked on manuscript improvement.

-
- [1] V. M. Fridkin, The mechanism of the photodomain effect in SbSJ, *Ferroelectrics* **2**, 119 (1971).
- [2] V. M. Fridkin, A. A. Grekov, N. A. Kosonogov, and T. R. Volk, Photodomain effect in BaTiO₃, *Ferroelectrics* **4**, 169 (1972).
- [3] A. A. Bokov, V. M. Fridkin, M. A. Malitskaya, and I. P. Raevskij, Thermodynamics of antiferroelectrics-semiconductors, *Ferroelectrics* **48**, 287 (1983).
- [4] C. Blouzon, J.-Y. Chauleau, A. Mougin, S. Fusil, and M. Viret, Photovoltaic response around a unique 180° ferroelectric domain wall in single-crystalline BiFeO₃, *Phys. Rev. B* **94**, 094107 (2016).
- [5] V. A. Stoica, N. Laanait, C. Dai, Z. Hong, Y. Yuan, Z. Zhang, S. Lei, M. R. McCarter, A. Yadav, A. R. Damodaran, S. Das, G. A. Stone, J. Karapetrova, D. A. Walko, X. Zhang, L. W. Martin, R. Ramesh, L.-Q. Chen, H. Wen, V. Gopalan, and J. W. Freeland, Optical creation of a supercrystal with three-dimensional nanoscale periodicity, *Nat. Mater.* **18**, 377 (2019).
- [6] T. Yang and L.-Q. Chen, Dynamical phase-field model of coupled electronic and structural processes, *npj Comput. Mater.* **8**, 130 (2022).
- [7] T. Yang, C. Dai, and L.-Q. Chen, Thermodynamics of light-induced nanoscale polar structures in ferroelectric superlattices, *Nano Lett.* **23**, 2551 (2023).
- [8] Y. Y. Liu, Z. Q. Liu, Y. Q. Wang, Y. Zhou, Y. Qin, H. P. Lv, P. F. Li, X. G. Chen, X. J. Song, and Y. Ai, Light-driven domain switching on a photochromic ferroelectric, *Cryst. Growth Des.* **23**, 2602 (2023).
- [9] S. M. Sze, *Physics of Semiconductor Devices*, 2nd ed. (Wiley-Interscience, New York, 1981).
- [10] A. I. Anselm, *Introduction to Semiconductor Theory* (Mir, Moscow, 1981).
- [11] M. R. Wagner, G. Callsen, J. S. Reparaz, R. Kirste, A. Hoffmann, A. V. Rodina, A. Schleife, F. Bechstedt, and M. R. Phillips, Effects of strain on the valence band structure and exciton-polariton energies in ZnO, *Phys. Rev. B* **88**, 235210 (2013).
- [12] W.-J. Yin, S. Chen, J.-H. Yang, X.-G. Gong, Y. Yan, and S.-H. Wei, Effective band gap narrowing of anatase TiO₂ by strain along a soft crystal direction, *Appl. Phys. Lett.* **96**, 221901 (2010).
- [13] A. N. Morozovska, R. K. Vasudevan, P. Maksymovych, S. V. Kalinin, and E. A. Eliseev, Anisotropic conductivity of uncharged domain walls in BiFeO₃, *Phys. Rev. B* **86**, 085315 (2012).
- [14] N. Balke, B. Winchester, W. Ren, Y. H. Chu, A. N. Morozovska, E. A. Eliseev, M. Huijben, R. K. Vasudevan, P. Maksymovych, J. Britson, and S. Jesse, Enhanced electric conductivity at ferroelectric vortex cores in BiFeO₃, *Nature Phys.* **8**, 81 (2012).
- [15] Y. Zhang, H. Lu, X. Yan, X. Cheng, L. Xie, T. Aoki, L. Li, C. Heikes, S. P. Lau, D. G. Schlom, L. Q. Chen, A. Gruverman, and X. Pan, Intrinsic conductance of domain walls in BiFeO₃, *Adv. Mater.* **31**, 1902099 (2019).
- [16] A. Bhatnagar, A. R. Chaudhuri, Y. H. Kim, D. Hesse, and M. Alexe, Role of domain walls in the abnormal photovoltaic effect in BiFeO₃, *Nat. Commun.* **4**, 2835 (2013).
- [17] J. Mangeri, O. Heinonen, D. Karpeyev, and S. Nakhmanson, Influence of elastic and surface strains on the optical properties of semiconducting core-shell nanoparticles, *Phys. Rev. Appl.* **4**, 014001 (2015).
- [18] K. Co, S. Pamir Alpay, S. Nakhmanson, and J. Mangeri, Surface charge mediated polar response in ferroelectric nanoparticles, *Appl. Phys. Lett.* **119**, 262903 (2021).
- [19] G. Catalan, J. Seidel, R. Ramesh, and J. F. Scott, Domain wall nanoelectronics, *Rev. Mod. Phys.* **84**, 119 (2012).
- [20] P. Johari and V. B. Shenoy, Tuning the electronic properties of semiconducting transition metal dichalcogenides by applying mechanical strains, *ACS Nano* **6**, 5449 (2012).
- [21] S. Kang, S. Jeon, S. Kim, D. Seol, H. Yang, J. Lee, and Y. Kim, Tunable out-of-plane piezoelectricity in thin-layered MoTe₂ by surface corrugation-mediated flexoelectricity, *ACS Appl. Mater. Inter.* **10**, 27424 (2018).
- [22] J. Berry, S. Zhou, J. Han, D. J. Srolovitz, and M. P. Haataja, Dynamic phase engineering of bendable transition metal dichalcogenide monolayers, *Nano Lett.* **17**, 2473 (2017).
- [23] Y. Vysochanskii, K. Glukhov, K. Fedyo, and R. Yevych, Charge transfer and anharmonicity in Sn₂P₂S₆ ferroelectrics, *Ferroelectrics* **414**, 30 (2011).
- [24] Y. M. Vysochanskii, V. Yu. Slyvka, S. I. Perechinsky, B. M. Koperles, M. I. Gurzan, and D. V. Chepur, The influence of lighting on the soft mode and dielectric properties Sn₂P₂S₆, *Ukr. J. Phys.* **25**, 281 (1980).
- [25] Y. W. Cho, S.-Kyung Choi, and Y. M. Vysochanskii, Photovoltaic effect of Sn₂P₂S₆ ferroelectric crystal and ceramics, *J. Mater. Res.* **16**, 3317 (2001).
- [26] M. Sotome, M. Nakamura, J. Fujioka, M. Ogino, Y. Kaneko, T. Morimoto, Y. Zhang, M. Kawasaki, N. Nagaosa, Y. Tokura, and N. Ogawa, Ultrafast spectroscopy of shift-current in ferroelectric semiconductor Sn₂P₂S₆, *Appl. Phys. Lett.* **114**, 151101 (2019).
- [27] S. M. Neumayer, N. Bauer, S. Basun, B. S. Conner, M. A. Susner, M. O. Lavrentovich, and P. Maksymovych, Dynamic stabilization of metastable states in triple-well ferroelectric Sn₂P₂S₆, *Adv. Mater.* **35**, 2211194 (2023).

- [28] See Supplemental Material at <http://link.aps.org/supplemental/10.1103/PhysRevB.109.045434> for calculation details and auxiliary figures.
- [29] A. K. Tagantsev and G. Gerra, Interface-induced phenomena in polarization response of ferroelectric thin films, *J. Appl. Phys.* **100**, 051607 (2006).
- [30] Y. M. Vysochanskii, M. M. Mayor, V. M. Rizak, V. Yu. Slivka, and M. M. Khoma, The tricritical Lifshitz point on the phase diagram of $\text{Sn}_2\text{P}_2(\text{Se}_x\text{S}_{1-x})_6$, *Sov. J. Exp. Theor. Phys.* **95**, 1355 (1989).
- [31] A. Kohutych, R. Yevych, S. Perechinskii, V. Samulionis, J. Banys, and Yu. Vysochanskii, Sound behavior near the Lifshitz point in proper ferroelectrics, *Phys. Rev. B* **82**, 054101 (2010).
- [32] Y. Shi and L.-Q. Chen, Current-driven insulator-to-metal transition in strongly correlated VO_2 , *Phys. Rev. Appl.* **11**, 014059 (2019).
- [33] M. Qin, K. Yao, Y. C. Liang, and S. Shannigrahi, Thickness effects on photoinduced current in ferroelectric $(\text{Pb}_{0.97}\text{La}_{0.03})(\text{Zr}_{0.52}\text{Ti}_{0.48})\text{O}_3$ thin films, *J. Appl. Phys.* **101**, 014104 (2007).
- [34] M. Qin, K. Yao, and Y. C. Liang, Photovoltaic characteristics in polycrystalline and epitaxial $(\text{Pb}_{0.97}\text{La}_{0.03})(\text{Zr}_{0.52}\text{Ti}_{0.48})\text{O}_3$ ferroelectric thin films sandwiched between different top and bottom electrodes, *J. Appl. Phys.* **105**, 061624 (2009).
- [35] M. Razeghi and A. Rogalski, Semiconductor ultraviolet detectors, *J. Appl. Phys.* **79**, 7433 (1996).
- [36] Y. Shi and L.-Q. Chen, Spinodal electronic phase separation during insulator-metal transitions, *Phys. Rev. B* **102**, 195101 (2020).
- [37] I. P. Batra, P. Wurfel, and B. D. Silverman, New type of first-order phase transition in ferroelectric thin films, *Phys. Rev. Lett.* **30**, 384 (1973).
- [38] P. Wurfel and I. P. Batra, Depolarization effects in thin ferroelectric films, *Ferroelectrics* **12**, 55 (1976).
- [39] M. Stengel and N. A. Spaldin, Origin of the dielectric dead layer in nanoscale capacitors, *Nature (London)* **443**, 679 (2006).
- [40] M. Stengel, D. Vanderbilt, and N. A. Spaldin, First-principles modeling of ferroelectric capacitors via constrained displacement field calculations, *Phys. Rev. B* **80**, 224110 (2009).
- [41] J. Wang, A. K. Tagantsev, and N. Setter, Size effect in ferroelectrics: Competition between geometrical and crystalline symmetries, *Phys. Rev. B* **83**, 014104 (2011).
- [42] A. K. Tagantsev, G. Gerra, and N. Setter, Short-range and long-range contributions to the size effect in metal-ferroelectric-metal heterostructures, *Phys. Rev. B* **77**, 174111 (2008).
- [43] J. Junquera and P. Ghosez, Critical thickness for ferroelectricity in perovskite ultrathin films, *Nature (London)* **422**, 506 (2003).
- [44] L. D. Landau and I. M. Khalatnikov, On the anomalous absorption of sound near a second order phase transition point, *In Dokl. Akad. Nauk SSSR* **96**, 496 (1954).
- [45] Y. Rong, K. L. Fangmin Guo, R. Kou, J. Chen, Y. Ren, and X. Xing, Tailoring negative thermal expansion in ferroelectric $\text{Sn}_2\text{P}_2\text{S}_6$ by lone-pair cations, *J. Phys. Chem. C* **121**, 1832 (2017).
- [46] A. Anema, A. Grabar, and T. Rasing, The nonlinear optical properties of $\text{Sn}_2\text{P}_2\text{S}_6$, *Ferroelectrics* **183**, 181 (1996).
- [47] Y. Tyagur, I. Tyagur, A. Kopal, L. Burianova, and P. Hana, Dielectric and piezoelectric properties of $\text{Sn}_2\text{P}_2\text{S}_6$ single crystals, *Ferroelectrics* **320**, 35 (2005).
- [48] Y. Tyagur, Spontaneous polarization in $\text{Sn}_2\text{P}_2\text{S}_6$ ferroelectric single crystals, *Ferroelectrics* **345**, 91 (2006).
- [49] O. Mys, I. Martynyuk-Lototska, A. Grabar, and R. Vlokh, Acoustic and elastic properties of $\text{Sn}_2\text{P}_2\text{S}_6$ crystals, *J. Phys.: Condens. Matter* **21**, 265401 (2009).
- [50] R. M. Yevych, Yu. M. Vysochanskii, M. M. Khoma, and S. I. Perechinskii, Lattice instability at phase transitions near the Lifshitz point in proper monoclinic ferroelectrics, *J. Phys.: Condens. Matter* **18**, 4047 (2006).
- [51] V. M. Rizak, I. M. Rizak, S. I. Perechinskii, Yu. M. Vysochanskii, and V. Yu. Slivka, Effect of the uniaxial compression on the phase transitions in $\text{Sn}_2\text{P}_2\text{S}_6$ -type ferroelectrics, *Physica Status Solidi* **183**, 97 (1994).
- [52] A. A. Volkov, V. G. Kozlov, N. I. Afanasjeva, A. A. Grabar, Y. M. Vysochanskii, and V. Y. Slivka, Low frequency modes in infrared spectra of $\text{Sn}_2\text{P}_2\text{S}_6$ crystal, *Fiz. Tverd. Tela* **25**, 2575 (1983).
- [53] J. Grigas, V. Kalesinskas, S. Lapinskas, and M. Gurzan, Microwave study of the soft ferroelectric mode in $\text{Sn}_2\text{P}_2\text{S}_6$ crystals, *Phase Transit.* **12**, 263 (1988).
- [54] A. N. Morozovska, Y. M. Fomichov, P. Maksymovych, Y. M. Vysochanskii, and E. A. Eliseev, Analytical description of domain morphology and phase diagrams of ferroelectric nanoparticles, *Acta Mater.* **160**, 109 (2018).
- [55] A. N. Morozovska, E. A. Eliseev, Yu. M. Vysochanskii, V. V. Khist, and D. R. Evans, Screening-induced phase transitions in core-shell ferroic nanoparticles, *Phys. Rev. Mater.* **6**, 124411 (2022).
- [56] A. N. Morozovska, M. D. Glinchuk, and E. A. Eliseev, Phase transitions induced by confinement of ferroic nanoparticles, *Phys. Rev. B* **76**, 014102 (2007).
- [57] V. A. Shchukin and D. Bimberg, Spontaneous ordering of nanostructures on crystal surfaces, *Rev. Mod. Phys.* **71**, 1125 (1999).
- [58] W. Ma, Surface tension and Curie temperature in ferroelectric nanowires and nanodots, *Appl. Phys. A* **96**, 915 (2009).
- [59] L. D. Landau, E. M. Lifshitz, and L. P. Pitaevskii, *Electrodynamics of Continuous Media*, 2nd ed. (Butterworth-Heinemann, Oxford, 1984).
- [60] E. A. Eliseev, A. N. Morozovska, S. V. Kalinin, Y. L. Li, Jie Shen, M. D. Glinchuk, L. Q. Chen, and V. Gopalan, Surface effect on domain wall width in ferroelectrics, *J. Appl. Phys.* **106**, 084102 (2009).
- [61] E. A. Eliseev, Y. M. Fomichov, S. V. Kalinin, Yu. M. Vysochanskii, P. Maksymovich, and A. N. Morozovska, Labyrinthine domains in ferroelectric nanoparticles: Manifestation of a gradient-induced morphological phase transition, *Phys. Rev. B* **98**, 054101 (2018).
- [62] E. A. Eliseev, A. V. Semchenko, Y. M. Fomichov, M. D. Glinchuk, V. V. Sidsky, V. V. Kolos, Yu. M. Pleskachevsky, M. V. Silibin, N. V. Morozovsky, and A. N. Morozovska, Surface and finite size effects impact on the phase diagrams, polar and dielectric properties of $(\text{Sr,Bi})\text{Ta}_2\text{O}_9$ ferroelectric nanoparticles, *J. Appl. Phys.* **119**, 204104 (2016).

- [63] A. N. Morozovska, E. A. Eliseev, M. E. Yeliseiev, Yu. M. Vysochanskii, and D. R. Evans, Stress-induced transformations of polarization switching in CuInP_2S_6 nanoparticles, *Phys. Rev. Appl.* **19**, 054083 (2023).
- [64] V. Liubachko, A. Oleaga, A. Salazar, R. Yevych, A. Kohutych, and Y. Vysochanskii, Phase diagram of ferroelectrics with tricritical and Lifshitz points at coupling between polar and antipolar fluctuations, *Phys. Rev. B* **101**, 224110 (2020).
- [65] <https://www.wolfram.com/mathematica>.